Seismo-acoustic wavefield at Popocatépetl volcano, Mexico captured by a temporary broadband network from 2021 to 2022.

Gerardo Mendo-Pérez[1***], Alejandra Arciniega-Ceballos[2], Robin S. Matoza[3], Alejandro Rosado-Fuentes[4], Richard W. Sanderson[5], Miranda R. Claypool[3]

1. Earthquake Research Institute, The University of Tokyo, Japan.
2. Departamento de Vulcanologia, Instituto de Geofísica, Universidad Nacional Autónoma de México, Mexico.
3. Department of Earth Science and Earth Research Institute, University of California, Santa Barbara, USA.
4. Posgrado en Ciencias de la Tierra, Universidad Nacional Autónoma de México, Mexico.
5. Icelandic Meteorological Office, Iceland.

* Corresponding author
Email: gmendo91@eri.u-tokyo.ac.jp
**Former affiliation: Posgrado en Ciencias de la Tierra, Universidad Nacional Autónoma de México, Mexico.

Citation: Mendo-Pérez, G., A. Arciniega-Ceballos, R.S. Matoza, A. Rosado-Fuentes, R.W. Sanderson, M.R. Claypool (2024), Seismo-acoustic wavefield at Popocatépetl volcano, Mexico captured by a temporary broadband network from 2021 to 2022, Seismol. Res. Lett., 95, 2689–2706, doi:10.1785/0220240199

Abstract

Popocatépetl is a highly active stratovolcano in central Mexico with recurrent activity of Vulcanian-type explosions and frequent degassing. The proximity of Popocatépetl volcano to Mexico City, one of the most populated cities in the world, demands continuous monitoring to achieve an adequate volcano risk assessment. We present an overview of the first high-dynamic-range and high-broadband (0.01 – 200 Hz; 400 Hz sampling rate) seismo-acoustic network (PoPiNet), which we operated around Popocatépetl volcano from August 2021 until May 2022. Here we show preliminary results of the explosions recorded in September 2021. We deployed five seismo-acoustic stations within 4 – 25 km horizontal distance (range) from the vent. We identify infrasonic waveforms associated with tremor and explosions, with pressures ranging from 16 to 134 Pa and dominant frequencies between 0.2 – 5.0 Hz. The frequency content of the recorded signals at the closest stations to the volcano spans the sub-bass (20 - 60 Hz) and bass (60 – 250 Hz) ranges. The associated seismic signals of moderate explosions exhibit air-to-ground coupled waves with maximum coherence values at frequencies up to 5 and 25 Hz for the farthest and closest stations to the volcano, respectively. Conversely, we observe infrasound signal amplitudes from relatively small explosions reaching maximum pressures of 10 Pa that do not couple into the ground, even at the closest stations. These infrasound signals are associated with Type-I Long-Period (LP) events as reported in previous investigations. The waveform consistency suggests repetitive and non-destructive sources beneath the volcano.

Introduction

Popocatépetl volcano (19.0225° N, -98.6231° W, 5452 m.a.s.l.) is an andesitic-dacitic stratovolcano located in central Mexico. It is part of the Trans-Mexican Volcanic Belt (TMVB), a 1000-km wide zone where most of the volcanic activity in the country occurs and arises from the subduction of the Cocos Plate beneath the North American plate (Ferrari et al., 2012). Renewed activity was first observed in 1993 after 70 years of quiescence with increased seismic activity and gas emissions, followed one year later by small explosions at the crater (De la Cruz-Reyna and Siebe, 1997). The Popocatépetl activity is characterized by degassing accompanied by emissions of ash, Vulcanian-type explosions, and cycles of growth and destruction of lava domes (Arciniega-Ceballos et al., 2003; 2008; Gómez-Vázquez et al., 2016; Macías et al., 2020). Many human settlements have historically inhabited Popocatépetl volcano's surrounding areas due to fertile soils (Martin-Del Pozzo et al., 2016). Nowadays, Mexico City and Puebla City are located 76 km and 45 km from the crater, respectively, and more than 24 million inhabitants live in these cities (see Data and Resources).

Since 1994, Popocatépetl volcanic activity has been continuously monitored by the National Centre of Disaster Prevention (CENAPRED, for its acronym in Spanish) and the Institute of Geophysics, Universidad Nacional Autónoma de México (UNAM). Extensive research has been performed to understand the volcano dynamics using seismic, geodetic, geochemical, satellite monitoring, video surveillance, and experimental techniques (Alatorre-Ibargüengoitia and Delgado – Granados, 2006; Alatorre-Ibargüengoitia et al., 2012; 2019; Arciniega-Ceballos et al., 1999; 2000; 2003; 2008,

2012; Chouet et al., 2005; Cruz-Atienza et al., 2001; De la Cruz-Reyna et al., 2008, Gómez-Vázquez et al., 2016; Schaaf et al., 2005; Siebe et al., 2024; Sosa-Ceballos et al., 2012; 2015; and references therein).

Infrasound monitoring is frequently used for detecting, locating, and quantifying volcanic eruptive activity (Fee and Matoza, 2013; Matoza and Roman, 2022). The first attempt to observe acoustic waves emitted by Popocatépetl volcano was reported by Arámbula–Mendoza et al. (2013) using conventional microphones (flat frequency response 2 - 5 Hz) deployed at distances less than 5 km. Matoza et al. (2019) reported the first high-broadband seismo-acoustic measurements associated with Vulcanian explosions from Popocatépetl volcano through a four-element triangle-shaped infrasound array collocated with a broadband seismometer at 16 km SE from the vent. From this experiment, they identified five explosions associated with clear infrasound and air-to-ground coupled waves (AGCW) in seismic records. These waves have been observed in many other volcanoes (De Angelis et al., 2012; Fee et al., 2016; Garcés et al., 1999; Ichihara et al., 2021; Petersen and McNutt, 2007).

Mendo-Pérez et al. (2021) applied a template matching technique (Gibbons and Ringdal, 2006; Matoza et al., 2015) to systematically identify AGCW in the seismic records of the permanent seismic station PPIG located at 5 km NE to the vent. Despite the presence of strong microseismic noise with dominant periods between 2 and 20 s (Arciniega-Ceballos et al., 1999; 2003), explosions with associated AGCW were identified, and the source depth region was estimated between 130 and 800 m beneath the crater.

Although there is ongoing research into Popocatépetl volcano seismo-acoustic activity, no permanent infrasound networks exist in the area. Hence, the infrasound observations associated with its activity are scarce. Thus, in this work, we present the observations obtained from PoPiNet, the first ever high-quality high-broadband seismo-acoustic network deployed around Popocatépetl. Most of the conventional microphone's flat frequency response is limited to the acoustic range (20 Hz – 2 kHz). In contrast, the frequency response of high-broadband microphones ranges from 0.01 to 400 Hz, with sampling rates up to 800 Hz and a dynamic range of 109 dB; thereby, these capture information in both infrasound and acoustic ranges. The network comprised five seismo-acoustic stations installed 4 to 25 km from the vent. At each station, we installed a broadband infrasound sensor collocated with a broadband seismic sensor. The network continuously operated from August 2021 until May 2022. Three of the five stations (PICB, PIBV, PISP) were running with a sampling rate of 400 Hz, and the other two (PITC, PIAE) at 200 Hz, allowing us to retrieve infrasound signals associated with volcanic activity with wider frequency content. We present the features of each station, the characterization of each site, and some preliminary results obtained from PoPiNet database. We focus on the infrasound and seismic data of September 2021, when all stations were functioning normally, and the volcano presented visible activity. From the analyses of the high-quality dataset obtained, we will contribute to a better understanding of the generation and propagation of the seismo-acoustic wavefield, as well as its relation to Popocatépetl eruptive activity.

Seismo-acoustic network

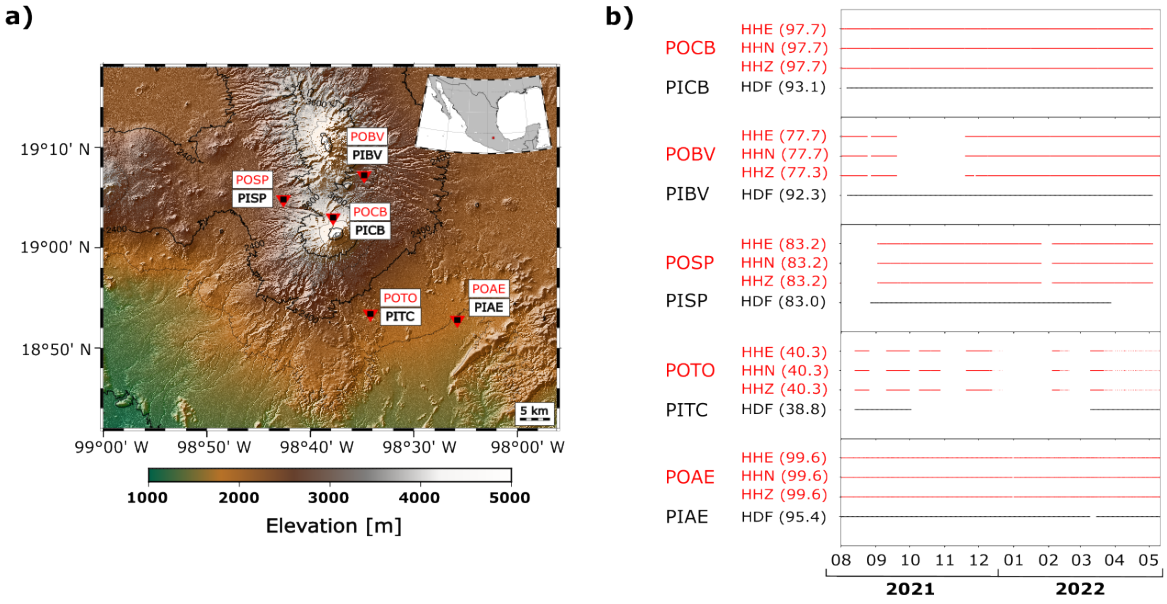

Figure 1. a) Map of Popocatépetl volcano and its surrounding area showing the seismo-acoustic network PoPiNet and its relative position in Mexico inlayed. b) Summary of infrasound (black color) and seismic (red color) available data through the entire PoPiNet operation period. The numbers inside the parenthesis indicate the percentage of available data per component.

The locations of the stations are shown in Figure 1a. From the closest to the farthest station to the volcano sites are named Cruz Blanca (POCB and PICB, 4 km N), San Pedro Nexapa (POSP and PISP, 11 km NW), Buenavista (POBV and PIBV, 11 km NE), Tochimilco (POTO and PITC,16 km SE), and Atlixco (POAE and PIAE, 25 km SE). Each station had both infrasound and seismic sensors, resulting in a total of 10 stations. From here onward, we use the site name to refer to the sensors collectively or the station name to indicate specifically the seismic or the infrasound sensor (Table S1 and S2 from

Supplemental Material). At all stations, both infrasound and seismic data were downloaded manually (i.e., no telemetry was utilized).

Figure 1b shows the data availability per station during the operation period. The network installation started in June 2021 and finished in September 2021, during the COVID-19 pandemics. Hence, many logistical challenges arose from shipping, customs, administrative, and fieldwork restrictions, delaying access to the sites, installation, and maintenance process. Some sites, such as Buenavista and Atlixco, were fully operational before August 2021. However, most of the stations started recording in August 2021. Thus, we determined this month as the starting period (Figure 1b). POCB station (Figure 1a and Table S1 from Supplemental Material) was installed in November 2019, and POBV station which is part of another seismic network from the Institute of Geophysics, UNAM (Figure 1a and Table S1 from Supplemental Material). Both stations are still in operation.

Four of the five seismic sites consisted of the 120-s broadband seismometers Trillium 120-PA and Nanometrics Taurus digitizers with the sampling rate set to 100 Hz. At Buenavista site, the seismic equipment is a broadband posthole seismometer Trillium PH-120 and 24-bit Omnirecs DiGOS DATA-CUBE digitizer sampling at 100 Hz. Regarding the infrasound equipment, we installed two types of high-broadband sensors: Hyperion IFS-3111 +/- 500 Pa and Chaparral Physics Model 60 UHP +/- 1000 Pa. Infrasound waveform data were recorded using 24-bit Omnirecs DiGOS DATA-CUBE digitizers. Previous observations of acoustic signals radiated by explosions of

158 Popocatépetl volcano extend to the sub-bass range showing high-amplitude noise
159 present up to a Nyquist frequency of 100 Hz (Matoza et al., 2019). Pushing this further,
160 we set the sampling rate to 400 Hz at the closest stations to the vent (distance ≤ 11 km)
161 and at the rest of the stations to 200 Hz. The distance between the infrasound and seismic
162 stations differs per site. In Cruz Blanca, San Pedro Nexapa, and Tochimilco sites, the
163 distance is less than 3 m, whereas at Atlixco and Buenavista sites, the distances are 20
164 m and 70 m, respectively. More information summarizing the features of the seismic and
165 infrasound equipment deployed at each site is in Tables S1 and S2 in Supplemental
166 Material.
167
168 We installed the seismic sensors at 1-m depth vaults. At the end of the project, all
169 materials were removed and recycled. The digitizers and the power supply system of the
170 seismic stations were placed at the surface next to the sensor spots inside metallic
171 enclosures (Figures S1c and S1f from Supplemental Material). For the infrasound, the
172 digitizer, the sensor, and the power supply system were installed inside plastic (Figure
173 S1b) or metallic (Figure S1e from Supplemental Material) enclosures. In both cases, the
174 enclosures were covered by plastic covers to prevent water filtration, extreme weather
175 changes and bugs. A small hose connected the enclosure walls and the infrasound
176 sensor to port to the ambient atmosphere. Two types of internal hose attachments were
177 used: garden hose thread attachment and ½" National Pipe Taper (NPT) thread
178 attachment for the Chaparral and Hyperion infrasound sensors, respectively. At the Cruz
179 Blanca site, the infrasound enclosures operated inside a small cabin of the Institute of

180 Geophysics, UNAM (Figure S1a from Supplemental Material). Hence, we adapted an
181 extra 30 cm-long transparent garden hose.
182
183 **Ambient noise across PoPiNet stations**
184
185 We first estimated the noise levels at each site by estimating Probabilistic Power Spectral
186 Density (PPSD) curves of both infrasound and seismic data according to the method
187 proposed by McNamara and Bulland (2004). We extracted one-hour segments from 24-
188 hour vertical seismic and infrasound traces with an overlap of 50% between segments.
189 Average PPSDs were estimated in 1/8 octave bands to reduce the number of frequencies
190 to process. Incomplete seismic records due to station maintenance and/or data retrieval
191 were not considered to estimate PPSD.
192
193 The seismic and infrasound PPSD curves are shown in Figure 2. Focusing on the seismic
194 PPSD (Figure 2, left column), it is common to observe signals with frequencies between
195 0.1 and 1.0 Hz at all stations. At the closest stations (POCB, POBV), an increase in the
196 probability of occurrence of signals with dominant frequencies between 0.01 – 0.3 Hz is
197 also observed. However, at the rest of the stations (POSP, POTO, POAE), the probability
198 of the occurrence of signals with dominant frequencies above 1 Hz up to Nyquist
199 frequency increases.
200

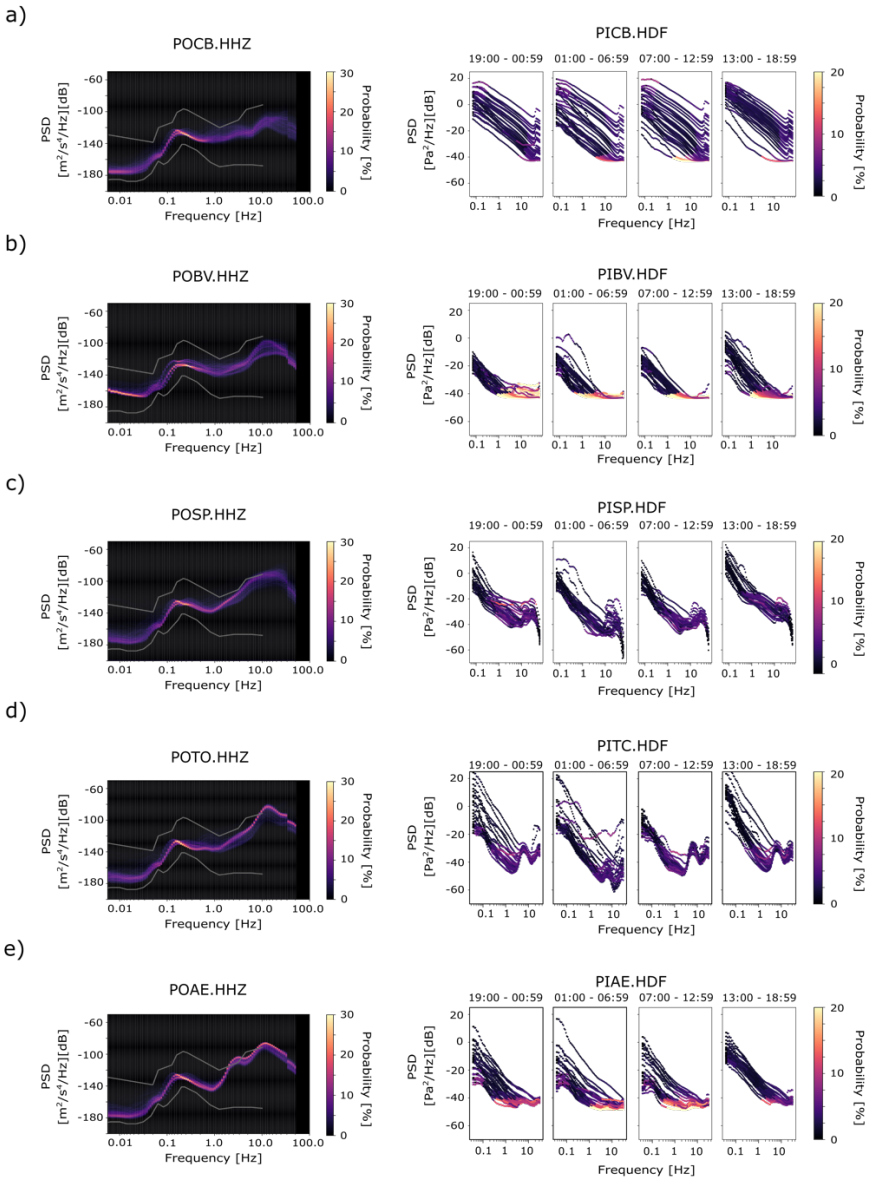

Figure 2. Probabilistic Power Spectral Density (PPSD) noise curves from a) Cruz Blanca (POCB, PICB), b) Buenavista (POBV, PIBV), c) San Pedro Nexapa (POSP, PISP), d) Tochimilco (POTO, PITC), and e) Atlixco (POAE, PIAE) sites. The left column corresponds to the seismic PPSD curves, and the right column corresponds to the infrasound PPSD curves. Seismic PPSD curves were calculated using the vertical seismic traces of September 2021. In the infrasound PPSD curves, Mexican Central Day Time (CDT) (UTC - 5) is indicated at the top of each panel. All curves were calculated using 3600 s time windows with 50% overlap.

Moving to the infrasound PPSD curves (Figure 2, right column), the PPSD estimation was performed in four-time intervals corresponding to Mexico Central Day Time (UTC – 5): 19:00 h – 00:59 h, 01:00 – 06:59 h, 07:00 – 12:59 h, and 18:00 – 23:59 13:00 – 18:59 h. PICB and PIAE stations present the highest power curves (maximum between 10 – 20 Pa^2/Hz). The signals with the highest probabilities of occurrence (10 – 20%) have dominant frequencies approximately above 1 Hz, up to Nyquist frequency. At PICB station, these signals occur between 01:00 h to 12:59 h; at PIBV during the day and night; and at PIAE station, between 19:00 h and 12:59 h. At PISP and PITC stations, the signals with dominant frequencies above 1 Hz have relatively less probability of occurrence (6 – 10%). The comparison between the average infrasound PPSD curves can be found in Figure S2 from Supplemental Material.

Additionally, we estimated Power Spectral Density (PSD) spectrograms of the infrasound records from 2021-09-01 until 2022-05-04 of PICB, PIBV, PISP, and PIAE stations (Figure 3). PITC station traces were excluded due to wide time gaps in data (Figure 1b). For this analysis, the infrasound traces were concatenated and downsampled to 10 Hz. The spectrograms show that the frequency content of the infrasound traces rises above 1 Hz in all stations. Except for the PICB station, the dominant frequencies lie in the frequency bandwidth of 0.01 – 0.1 Hz. During the eight months of operation, PICB was strongly affected by a high-frequency noise source (> 1 Hz), resulting in higher noise levels. We observe that high power values can be still seen in the 1 – 5 Hz band (Figure 3).

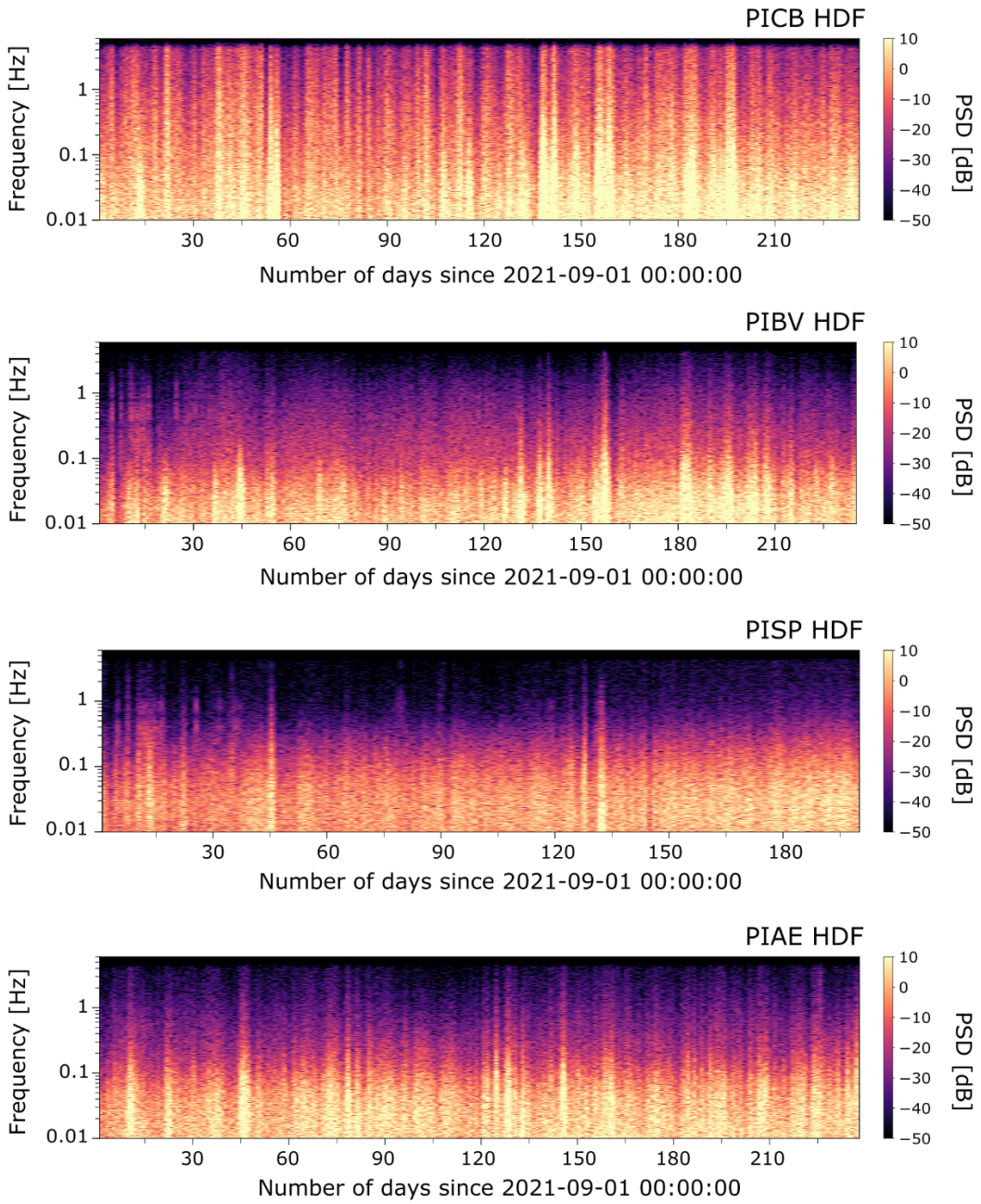

Figure 3. Infrasound Power Spectral Density (PSD) plots for a) PICB, b) PIBV, c) PISP, and d) PIAE stations for 2021-09-01 00:00:00 to 2022-05-04 00:00:00. All infrasound traces were downsampled to 10 Hz, and for the PSD calculation we fixed the window size of approximately 67 hours with an overlap of 50%.

Due to downsampling, it is not possible to see further but PPSD estimations shows that noise may extend to higher frequencies (Figure 2a). One factor that accounts for the noise in PICB traces is the lack of vegetation due to the station altitude (more than 4000 m.a.s.l.) that serves as a natural noise filter. The traces with dominant frequencies above 1 Hz may also be associated with human activity at PISP, PIBV, and PIAE stations.

Seismo-acoustic signals

The volcanic activity of Popocatépetl consists of episodes of sustained degassing and a continuous cycle of growth and destruction of lava domes (Arciniega-Ceballos et al., 1999; 2000; 2003; 2005; 2008; 2012; De la Cruz-Reyna & Siebe, 1997; Gómez-Vazquez et al., 2016; Macías et al., 2020; Ramírez – Uribe et al., 2022). The volcanic activity interacts with the atmosphere and the surface, resulting in various infrasound and seismic signals with different frequency ranges (Chouet, 2003; Fee & Matoza, 2013; Johnson & Ripepe, 2011). During the period of PoPiNet operation, Popocatépetl eruptive activity was mainly dominated by degassing and small to mild explosions. In this section, we will describe the observed signals associated with such volcanic activity. Although we present records from all stations throughout the section, most traces belong to the infrasound station PICB and the seismic station POCB, both collocated at 4 km N from the vent (Figure 1a, Table S1 and S2 from Supplemental Material). As previously stated, we focus on conspicuous volcano activity occurred during September 2021 when all stations were operating normally.

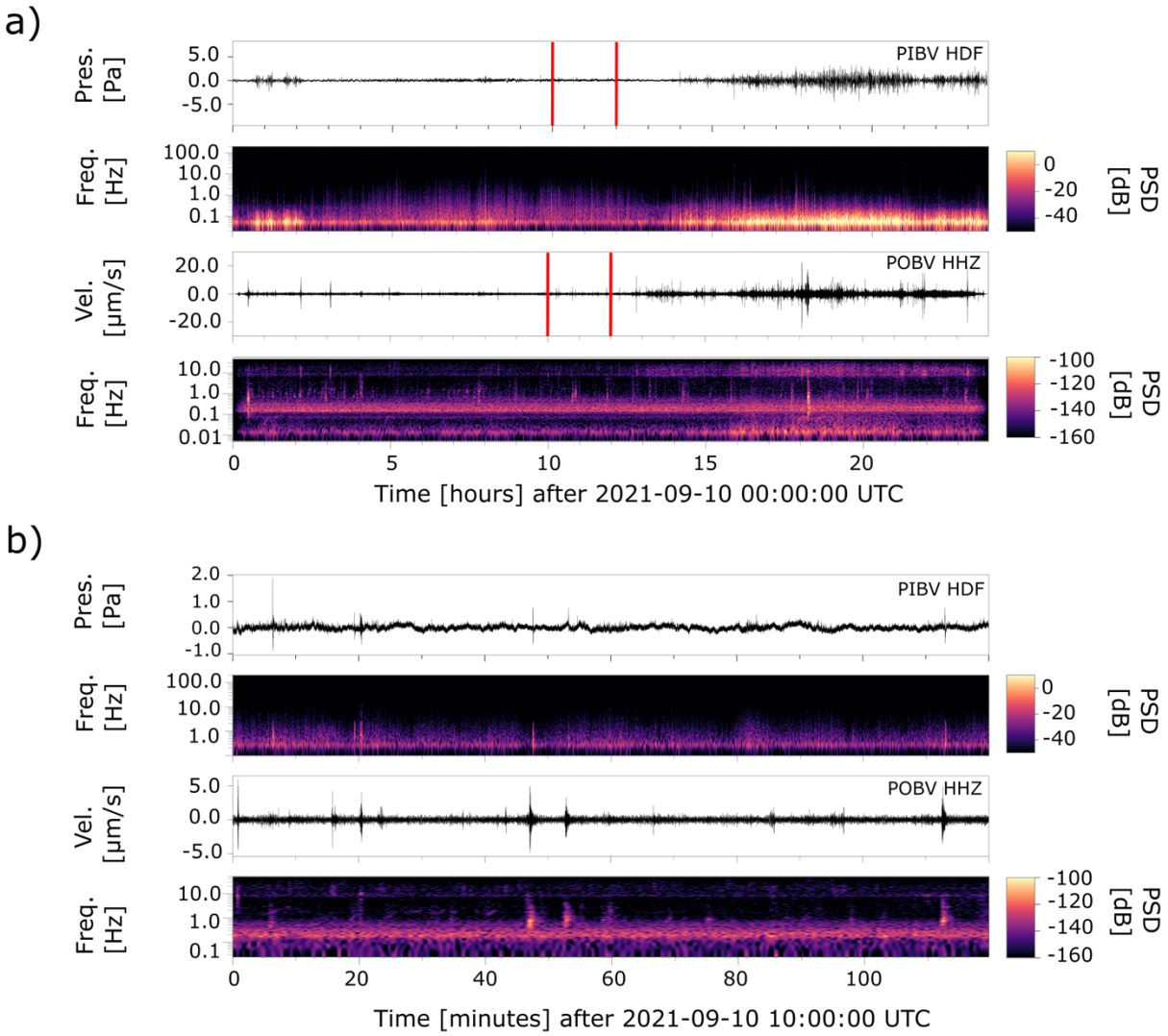

Figure 4. a) Infrasound (PIBV) and vertical seismic (POBV) traces and their associated spectrograms from the Buenavista site recorded in 2021–09–10 with a duration of 24 hours. b) A zoomed view of the record with a duration of 2 hours of both infrasound and seismic traces. The initial and end points of this zoom are pointed by red lines in a). The spectrograms were calculated using time windows of 204.8 s with a 50% overlap. The y-axis in both spectrograms is shown in logarithm scale.

Tremor and wind noise

Volcanic tremor can be defined as continuous vibration of the ground. Its duration can last from seconds to months and is commonly associated with sustained physical processes such as degassing and fluid movement beneath the ground (Chouet, 2003; Matoza and Roman, 2022; McNutt, 2005). Due to the ground-atmosphere coupling, tremor can occur in infrasonic traces (Matoza et al., 2014). This exhibits a wide range (broadband) of frequency content, a single dominant frequency (monochromatic), or the frequencies could change in time (gliding) (Chouet, 2003; Chouet and Matoza, 2013; Fee and Matoza, 2013; McNutt, 2005; Roman, 2017).

Figure 4 shows an example of broadband seismic tremor recorded at POBV station (11 km N of the vent, Figure 1) on 2021-09-10. We observe that the seismic tremor is accompanied by Long-Period (LP) events, small explosions, and gliding in the 0.1 - 10 Hz frequency range (Figure 4b, Figures S3 – S6 from Supplemental Material). Gliding at the seismic spectrogram is clearest at station POCB (Figures S3 and S4), but also can be observed at station POSP (Figure S5) and POTO (Figure S6). Seismic signals with peak frequency above 5 Hz are present at all stations and possibly are related to effects like wind noise and human activity. Infrasonic tremor was recorded at PIBV (Figure 4a), PISP, and PITC stations starting around 14 h and lasting around 7 hours with a dominant frequency between 0.05 – 1 Hz (Figure S4 - S6 from Supplemental Material). However, tremor cannot be observed at PICB station most likely due to the dominant wind noise,

whose frequency content rises above 10 Hz (Figure S3). Further work must be done to identify the source of these continuous signals.

Explosion signals

We run a template matching algorithm (Gibbons and Ringdal, 2006; Matoza et al., 2015; Mendo-Pérez et al., 2021) using the infrasound database of PICB station to identify waveforms related to explosions throughout the infrasound database. By visual inspection, as a template, we set the infrasound trace associated with the explosion that occurred on 2021-09-26 at 11:17:35 UTC. We divided infrasound traces into time windows of 60 s (the same length as the template) with a 50% overlap. The detected events are summarized in Table S3 from Supplemental Material. We identified 35 events with correlation coefficients between 0.51 and 0.96, and peak pressure between 7.96 and 134.52 Pa. Of these 35 events, 16 occurred in September 2021. Hence, from this point, we focus on the infrasound and seismic records associated with the detected explosions occurred in September 2021.

From this selection, infrasound and seismic signals of two Vulcanian explosions are shown in Figure 5. The infrasound waveforms in Figure 5a have peak pressure values, from the closest to the farthest station, of approximately 139, 50, 30, 24, and 20 Pa. The rapid onset of the signal is followed by an asymmetric waveform with exponential decay of the amplitude. This signal lasts between 7 and 10 seconds at most stations. The infrasound waveform shape is more consistent in PICB, PIBV and PIAE stations than

PISP and PITC stations. In contrast, the infrasound signals waveform of Figure 5b is like a single sharp pulse with pressures of 46, 17, 19, 8, and 5 Pa. The signal duration ranges between 6 and 14 seconds. The waveform shape is consistent in all stations for this event except for PIBV station. Local site effects such as noise, vegetation, and atmospheric conditions may influence the observed infrasound waveform.

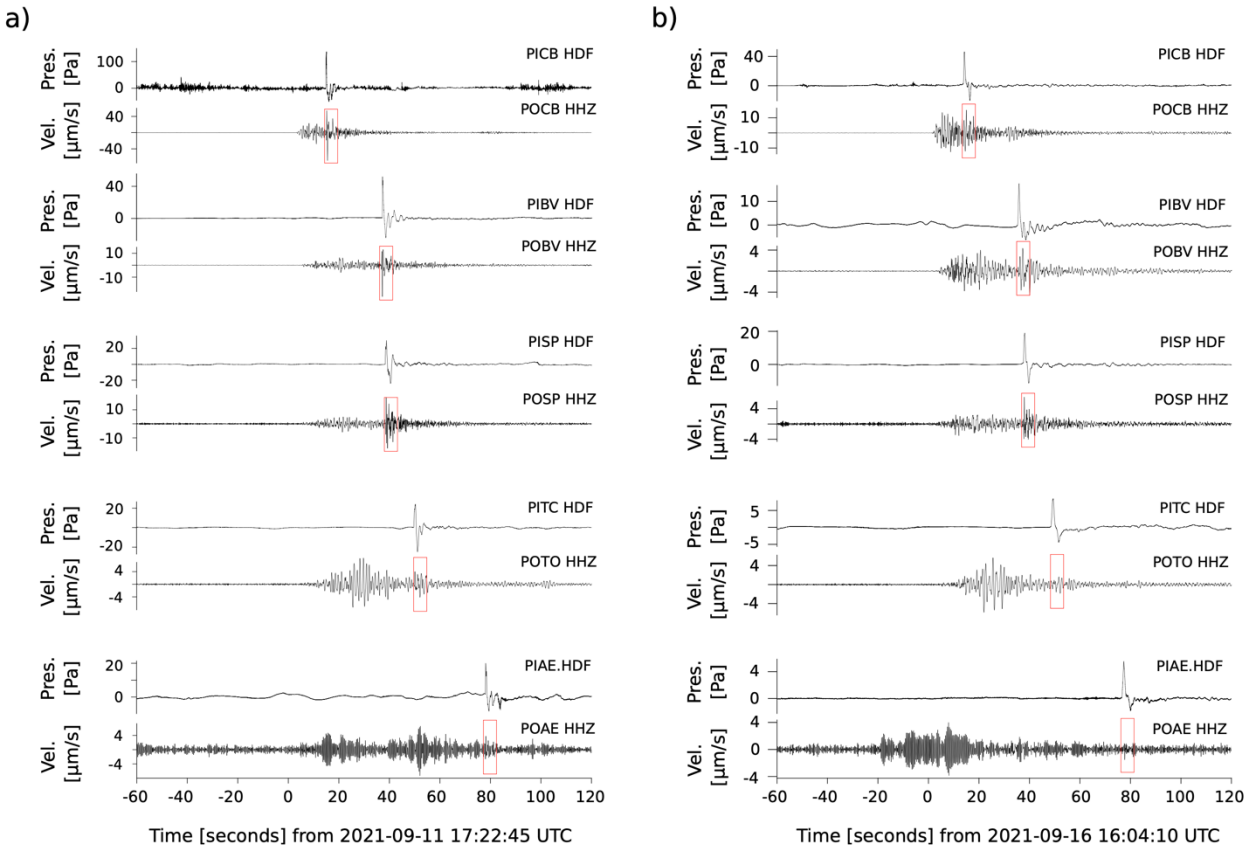

Figure 5. Infrasound and vertical seismic records of explosion quakes occurred on a) 2021-09-11 at 17:22:45 UTC and b) 2021-09-16 at 16:04:10 UTC. The station name is in the upper right corner of each panel. Seismic traces are filtered using a zero-phase band-pass Butterworth filter between 0.2 and 5.0 Hz.

Moving to the associated seismic signals (Figure 5, lower panels), two phases can be distinguished: 1) An initial seismic phase that extends from the P wave arrival time to the onset of the infrasound signal, and 2) air-to-ground coupled waves (AGCW) (De Angelis et al., 2012; Fee et al., 2016; Garcés et al., 2000; Ichihara et al., 2021; Matoza et al., 2019; Petersen and McNutt, 2007) whose arrival times match with the onset of the infrasound signals (Figure 5, red boxes in lower panels). The duration of the seismic phase differs per station: For both explosions (Figure 5), the duration is around 11 s at POCB, 31 s at POBV, 32 s at POSP, and 44 s at POTO. For the POAE station, the onset of the seismic signal is not easily identified, but the seismic phase could last around 50 s or longer. The absolute value of the maximum amplitude of the seismic phase of both explosions at all seismic stations lies between 3.5 – 10.5 μm/s. The AGCW is clearer at the stations closer to the volcano. In contrast, at the POAE station, the ACGW can be identified by bandpass filtering the trace and comparing it with the associated infrasound trace if the explosion is powerful enough. Note that the AGCW amplitude can be easily mistaken with the background noise at POAE station.

We perform Power Spectral Density (PSD) estimates of the infrasound traces associated with the explosion shown in Figure 5a to further show their spectral content (Figure 6). By means of comparison, we also estimate the noise PSD using the same window lengths as in the signal. The power difference between the signal PSD and noise PSD is approximately one order of magnitude at the frequency band below 10 Hz.

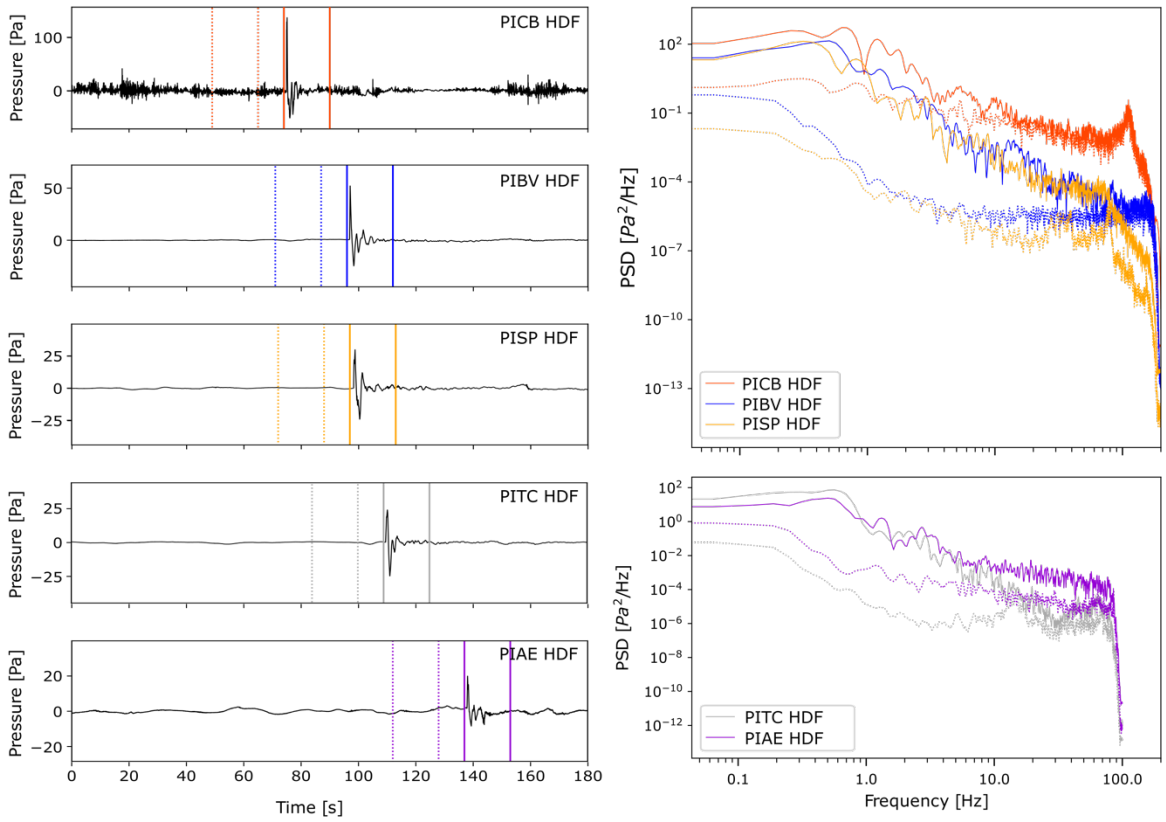

Figure 6. Infrasound waveforms (left column) and their associated Power Spectral Density (PSD) curves (right panel) of the 2021-09-11 at 17:22:45 UTC explosion (Figure 5a). The calculation of the PSD curves was performed using the Adaptive Sine Multitaper method (Prieto et al., 2009; Prieto, 2022), using 2 tapers and 4 adaptive steps as parameters to build the PSD. In the left column, the solid and dashed lines point to the limits of the time windows of the signal and noise, respectively. In the right column, the solid curves correspond to the infrasound signal, whereas the dashed curves correspond to the noise.

High-frequency roll-off can be seen in the PSDs associated with the signals at approximately 0.8 Hz. In contrast, high-frequency roll-off is not observed in the PSD associated with noise. The dominant spectral peaks of the infrasound signals at all stations are within 0.2 – 2.0 Hz. At frequencies above 10 Hz, the power difference between PSD curves decreases until reaching approximately the same values. Hence, at

high frequencies we have time windows where noise and signal component at the high frequency band. The signal's frequency content extends to the sub-bass (16 – 60 Hz) and bass (60 – 250 Hz) ranges. Matoza et al. (2019) first reported the presence of infrasound signals in the sub-bass range associated with Popocatépetl volcanic explosions. Increasing the sampling rate allowed us to observe that the explosions of Popocatépetl volcano produce pressure waves with frequency content within the audible range as well. Similar behavior of the PSD estimation can be observed at the infrasound traces associated with other explosions (Figure S7 from Supplemental Material).

As a complement, in the Supplemental Material Figures S8 – S10 shows the filtered infrasound signals in three different frequency bands: 0.01 – 10 Hz, 50 – 100 Hz, and 100 – 150 Hz. A signal with a sharp peak and duration of approximately 5 s can be observed at the same time position as the maximum peak of the filtered signal between 0.01 – 10 Hz. Only at PISP station, the waveform with a sudden increment in amplitude lasts up to 20 s approximately.

Seismo-acoustic coupling of Vulcanian explosion signatures

We calculate the coherence (Matoza and Fee, 2014) and cross-correlation function (CCF) (Ichihara et al., 2012) between the infrasound and seismic signals to determine if these are coupled and the extent of the coupling (Figure 7). These are calculated using infrasound and seismic traces of an explosion on 2021-09-11 at 17:17:45 UTC.

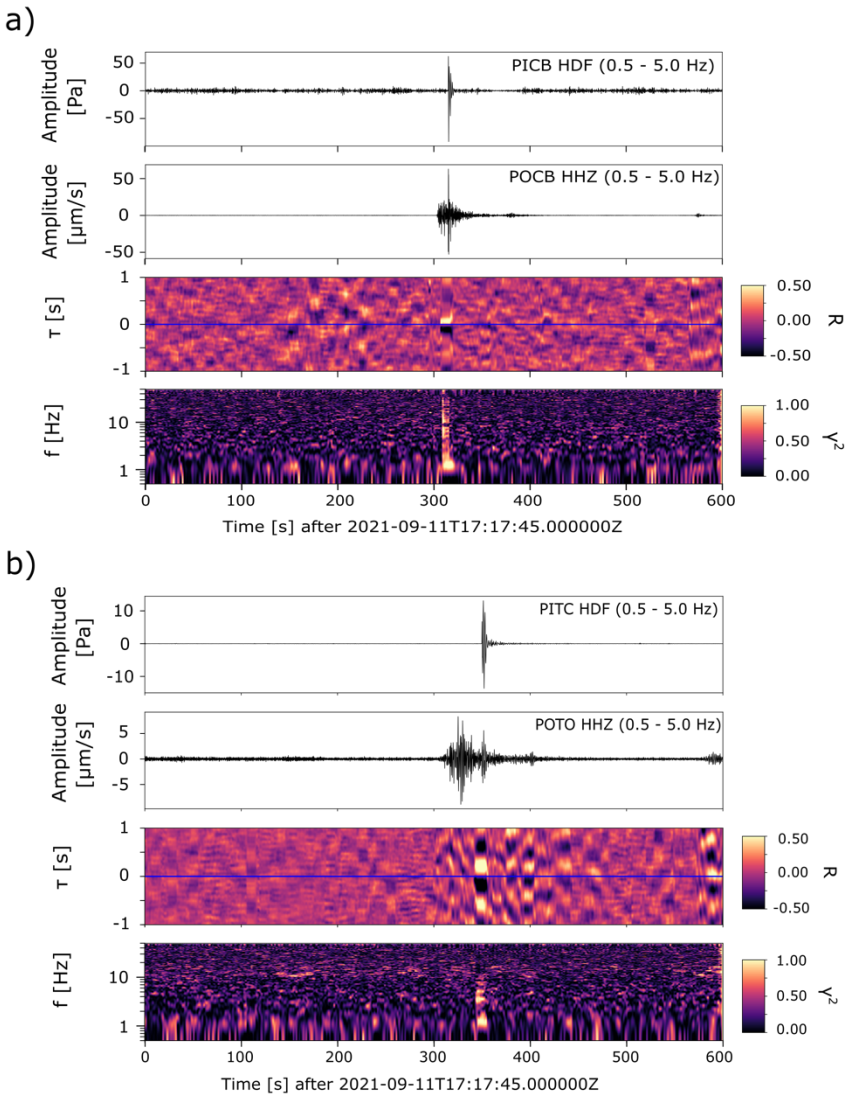

Figure 7. From upper to lower panels: Infrasound trace, vertical seismic trace, cross-correlation functions (CCF), and coherence associated with an event that occurred on 2021-09-11 at 17:17:45 UTC and recorded in a) Cruz Blanca and b) Tochimilco sites. Infrasound and vertical seismic traces were band-pass filtered between 0.5 and 5.0 Hz using a zero-phase band-pass Butterworth filter. We used time windows of 10 s with a 90% overlap between windows.

The results from Cruz Blanca and Tochimilco sites are shown in Figure 7a and 7b, respectively. The traces were filtered between 0.5 and 5.0 Hz to calculate the CCF. The

CCF is maximum at the time window where the infrasound wave and the AGCW coincide, appearing a characteristic seismo-acoustic coupling pattern where the maximum and minimum values are centered at time delay $\tau = 0$ between the infrasound and AGCW. The coherence is maximum between 0.5 – 5.0 Hz and extends to 30 Hz in the time window where both infrasound signal and AGCW coincide at Cruz Blanca site. In contrast, we observe that the coupling at frequencies up to 5 Hz at Tochimilco site. We perform the same calculations for the rest of the traces associated with the same explosion in the rest of the stations. At Buenavista site (Figure S11 from Supplemental Material) we observe the coupling at frequencies up to 25 Hz, as the same as Cruz Blanca. And at San Pedro and Atlixco (Figure S12 and Figure S13 from Supplemental Material) sites we observe that the frequency coupling is restricted to the 0.8 – 5 Hz band. Factors such as geometric spreading, anelastic attenuation, and scattering contribute to the attenuation of both acoustic and seismic signals when increasing the distance (Matoza and Roman, 2022), and the attenuation of the infrasound due to atmospheric absorption is low at the troposphere (Sutherland and Bass, 2004; Fee and Matoza, 2013). This suggests that the air-to-ground coupled waves can be observed at distances of several tens of kilometers, whereas acoustic waves coupling with frequency content in both infrasound and acoustic ranges can be distinguished at the closest sites to the volcano.

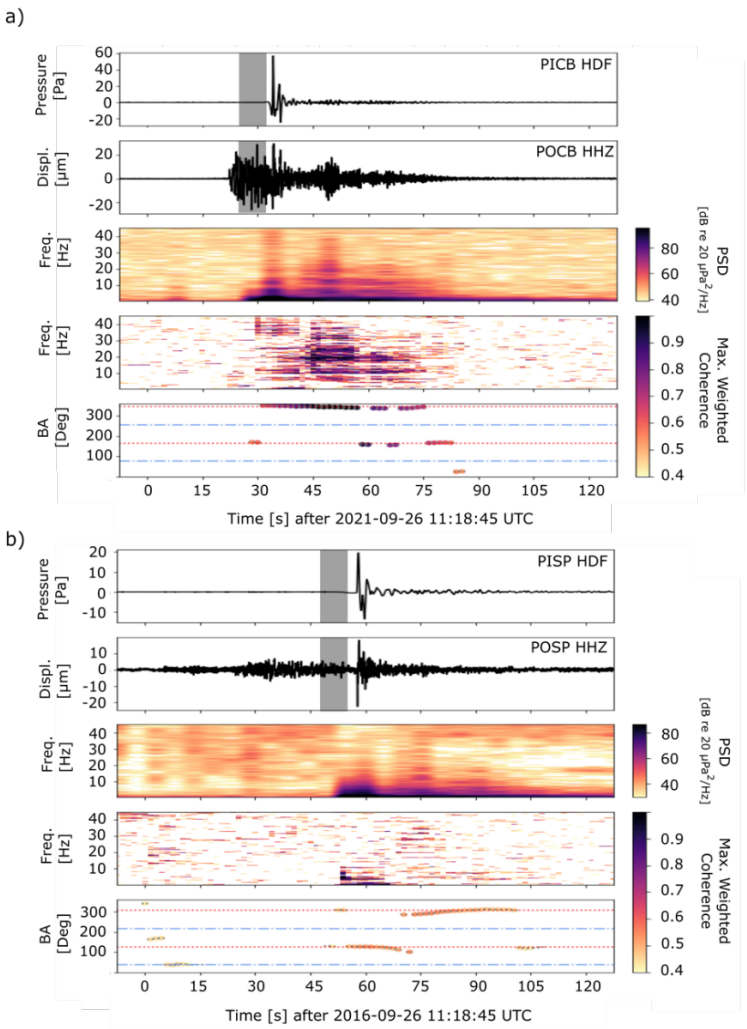

Figure 8. Estimation of the back-azimuth of the infrasound signal using the Transverse Coherence Minimization method (Bishop et al., 2023) using the infrasound and seismic signals from a) Cruz Blanca and b) Buenavista sites and recorded in 2021-09-26. From upper to lower panel: Infrasound and seismic signals filtered between a) 0.5 and 45 Hz and b) 0.3 – 10 Hz, PSD, coherence, and back-azimuth estimations. The corner frequencies were set based on the highest coherence between the infrasound and the seismic signal. We used time windows of 15 s with a 90% overlap for the coherence and PSD estimations. In the lowest panels of a) and b), the red dotted lines correspond to the azimuth and the backazimuth of the station, and the blue dot-dash lines correspond to the discrepancies between the azimuth and backazimuth by 90 degrees.

In addition, we estimated the back-azimuth of the infrasound signals using the Transverse Coherence Minimization (TCM) method (Bishop et al., 2023). This method estimates the direction of the wavefront by finding the minimum coherence between the transverse component of the seismic and the infrasound signal. The results obtained from the TCM using the signals associated with the explosion that occurred on 2021-09-26 (Figure 5a) are shown in Figure 8. We observe that at the time window where the infrasound and the AGCW coincide, the back-azimuth value is above 300 degrees in POCB station (Figure 8a) and approximately 100 degrees in POSP station. Note that the back-azimuth estimation at POCB station is associated with coherence above 0.9. In contrast, at POSP station the coherence is approximately 0.4, suggesting that the back-azimuth estimation uncertainty is higher at POSP station.

LP and VLP waveforms

It is common to observe in Popocatépetl seismic records the occurrence of Long-Period (LP) and Very-Long-Period (VLP) events (Arciniega-Ceballos et al., 1999; 2003; 2008; 2012). The most common interpretation for LP and VLP events is acoustic resonance and inertial forces generated by magma flow perturbations inside fluid-filled conduits, respectively (Arciniega-Ceballos et al. 2008; 2012; Chouet, 2003; Chouet et al., 2005; Chouet and Matoza, 2013). At Popocatépetl the inferred point source of LP seismicity is located at about 200 – 250 m below the crater floor (Arciniega - Ceballos et al., 2012), whereas considering the scattered LP hypocenter distribution these events may reach up to 2700 m down from the crater floor (Arciniega - Ceballos et al., 2008). This depth includes the VLP point sources where the centroid is located at 1500 m depth beneath

453 the crater floor (Chouet et al., 2005). Figure 9 shows examples of infrasound and seismic
454 signals associated with two events that occurred on 2021-09-10 and 2021-09-26. The
455 infrasound signals associated with these events are shown in Figure 9a (upper panels).
456 These signals present an impulsive pressure wave arrival, followed by a rapid amplitude
457 decay. The duration of these two events lies between 50 – 100 s, and their dominant
458 frequencies are between 0.5 and 5.0 Hz. The amplitude difference between the unfiltered
459 infrasound signals in Figure 9a is a factor of 80. After filtering, an infrasound Very-Long-
460 Period (iVLP) signal associated with the 2021-09-26 explosion appears in the 0.01 – 0.03
461 Hz frequency band with a dominant frequency of 0.02 Hz (Figure 9a, left column). The
462 iVLP are volcano infrasound signals with dominant frequencies (10 – 50 s) and are usually
463 associated with mild to large-scale eruptions (Fee et al., 2010; Yamada et al., 2016). No
464 clear infrasound VLP signal can be observed in the 2021-09-10 filtered trace (Figure 9a,
465 right column) in the same frequency range.

466

467 In the associated seismic records of each event can be observed the corresponding
468 seismic LP and VLP signals. The LP signals present impulsive arrival, followed by
469 oscillations that progressively decrease in amplitude and present dominant frequencies
470 ranging from 0.5 to 5.0 Hz (Figure 9b, middle panels). The associated VLP signal presents
471 durations of around 200 s with dominant periods of around 40 s and 60 s, right and left
472 columns, respectively (Figure 9b, lower panels). The dominant periods of these events
473 lie in the period range observed for VLP in previous studies (Chouet et al., 2005). These
474 waveforms look like the Type-I LP events commonly associated with ash emissions and
475 degassing activity (Arciniega–Ceballos et al., 2008, 2012).

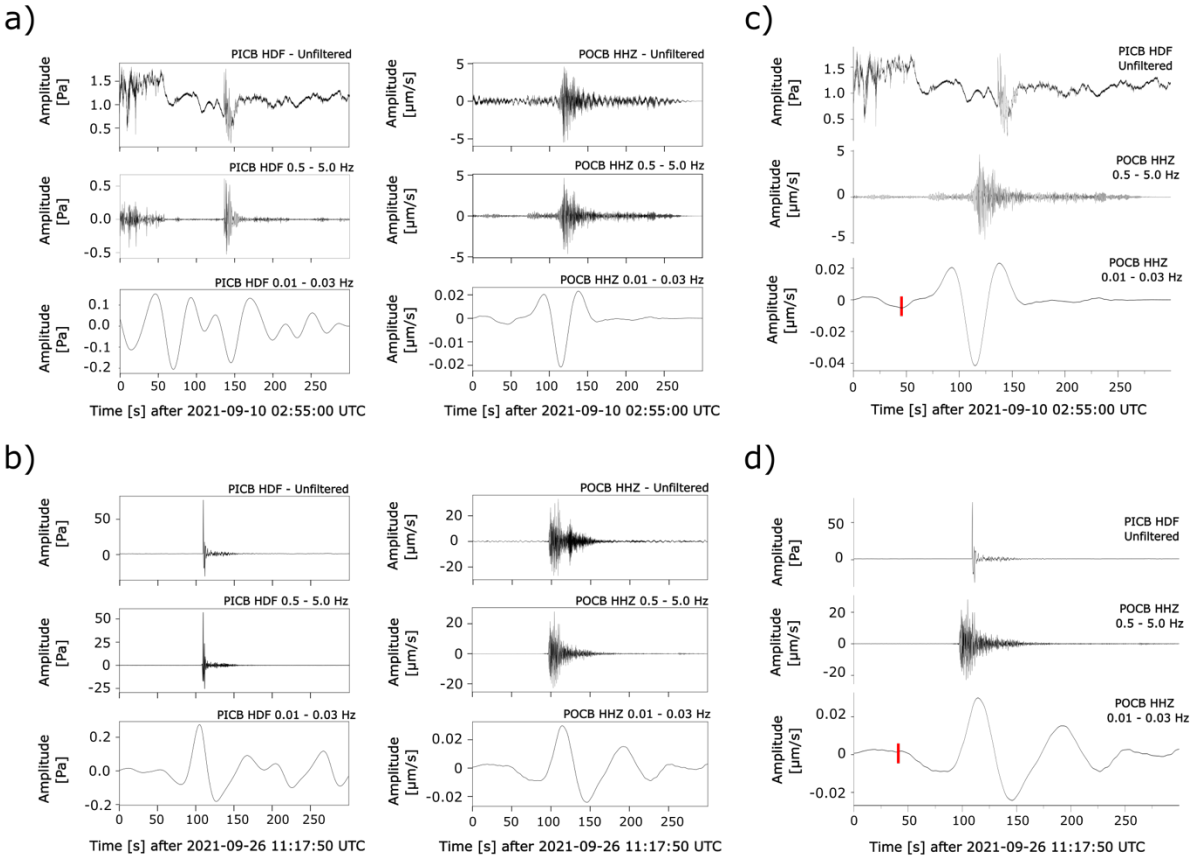

Figure 9. Infrasound and seismic signals recorded at Cruz Blanca site (PICB, POCB) associated with explosions that occurred on 2021-09-10 02:52:00 h (a, c) and 2021-09-26 11:17:00 h (b, d). In each subplot of a) and b), the upper panel shows unfiltered data, the middle panel shows bandpass-filtered signals in the 0.5 – 5.0 Hz range, and the lower panel shows bandpass-filtered signals between 0.01 – 0.03 Hz. The timing between the unfiltered infrasound, LP, and VLP signals of the explosions that occurred on 2021-09-10 and 2021-09-26 are shown in c) and d), respectively. The red line in c) and d) points to the onset of the VLP signal.

Finally, Figures 9c and 9d show the timing of occurrence of the infrasound, the LP, and VLP seismic signals associated with the explosions that occurred on 2021-09-10 and 2021-09-26, respectively. The LP event and its corresponding VLP signal appear at approximately 100 s in Figure 9c and 110 s in Figure 9d, before the infrasound signal. Although we observe differences in the arrival times the synchronization between the infrasound and seismic signals indicate that these were triggered by the source mechanism. Further work is aimed at analyzing the temporal variation of the seismo-acoustic source coupling and the estimation of the source parameters of the observed LP and VLP events within the operation period.

Discussion

We present the observations of infrasound and seismic signals recorded by the first high-dynamic range high-broadband seismo-acoustic network PoPiNet associated with volcanic activity of Popocatépetl. The sampling rate of the infrasound stations were set to 400 Hz at the stations whose distance is less than 12 km from the vent (PICB, PISP, PIBV), and the rest of the stations was set to 200 Hz (PITC, PIAE).

The observed infrasound waveforms related to the explosions (Figure 5) are classic explosion waves as observed at volcanoes worldwide such as Stromboli (Ripepe et al., 1996;), Sakurajima (Garcés et al., 1999; Fee et al., 2014), Tungurahua (Fee et al., 2010), Augustine (Caplan-Auberbach et al., 2010) and Yasur (Maher et al., 2022; Matoza et al., 2022), which present waveforms that reflects compression and rarefaction of the local

512 atmosphere (Fee and Matoza, 2013; Morrisey and Chouet, 1997; Yokoo et al., 2009).
513 PSD estimations and progressive filtering of the infrasound signals associated with
514 explosions reveal that the spectral content ranges from 0.1 Hz to 150 Hz (Figure 6).
515 Besides the signal content, at frequencies above 40 Hz, the shapes of the PSD are
516 complex, suggesting local effects, nonlinear propagation paths, and complex sources.
517
518 We identify AGCW from volcanic explosions in the associated seismic signals (Figure 5)
519 at up to 25 km and in frequencies from 0.2 to 5.0 Hz. The difference between the seismic
520 and AGCW arrival times increases with distance to the crater. When the distance
521 increases, the frequency range where the seismo-acoustic coupling exists is constrained
522 to 0.8 – 5 Hz frequency band. Matoza et al. (2019) first reported the presence of AGCW
523 in the vertical seismic displacement records associated with Popocatépetl volcano
524 explosions using a four-infrasound array collocated with a broadband seismic sensor at
525 16 km from the vent. They found that the coherence estimation between infrasound and
526 seismic signals shows that the seismo-acoustic coupling ranges up to 25 Hz. Conversely
527 in our study, we found that the coupling at such higher frequencies occur only at the
528 closest stations to the volcano. Although the Cruz Blanca recordings are affected by wind
529 effects and the surrounding landscape around the station, we interpret that the seismo-
530 acoustic coupling source above 10 Hz is related to volcanic activity.
531
532 We observed gliding tremor at all seismic stations, which has been reported in previous
533 works about tremor at Popocatépetl volcano (Arámbula-Mendoza et al., 2016; Roman,
534 2017). Along with the seismic tremor, the infrasound traces exhibit tremor below 0.1 Hz

(Figure 3). This observation is clearer at the PIBV station, which maintains relatively low noise levels (Figure 2b). In contrast, wind noise dominates PICB infrasound seismic records (Figures 2 - 4). Figure S15 from Supplemental Material shows the comparison between PSD from infrasound records with wind direction and speed recorded at Altzomoni on September 2021, a meteorological station located 16 km NW of Cruz Blanca site (see Data and Resources). We observe that at the periods where the wind direction has an approximate value of 100 degrees, the wind speed increases from an average value of 3.73 m/s to 10 - 15 m/s, and this roughly coincides with an increase in time windows where signal intensity and frequency content increases. Care must be taken with this last statement because wind speed and direction can drastically change from one point to another at high altitudes.

In addition, similar wind noise occurrences in infrasound traces are observed in other volcanic zones (Sanderson et al., 2021). In these cases, arrays of infrasound sensors and proper processing techniques are recommended to detect coherent signals from volcanic sources and determine wave parameters (Iezzi et al., 2022; Matoza et al., 2007; Matoza et al., 2009b).

Additionally, we performed a second template-matching-based search (Gibbons and Ringdal, 2006; Matoza et al., 2015; Mendo-Pérez et al., 2021) to identify only similar seismic waveforms associated with AGCW in POCB vertical seismic traces recorded in September 2021. The correlation coefficients are within the 0.53 – 0.91 range, and we set the detection threshold to 0.5. As templates, we used two 60-s long seismic traces:

the first template, T1, belongs to an explosion that occurred on 2021-09-02 at 02:36:08 h and contains an observable AGCW. The second template, T2, occurred on 2021-09-26 at 11:19:05 h (Figure 9b), and in contrast to T1, an AGCW cannot be seen in the seismic signals. The algorithm identified 24 events with a mean correlation coefficient of 0.58, where 7 events were similar to T1, and 17 events were similar to T2 (see Table S4 from the Supplemental Material).

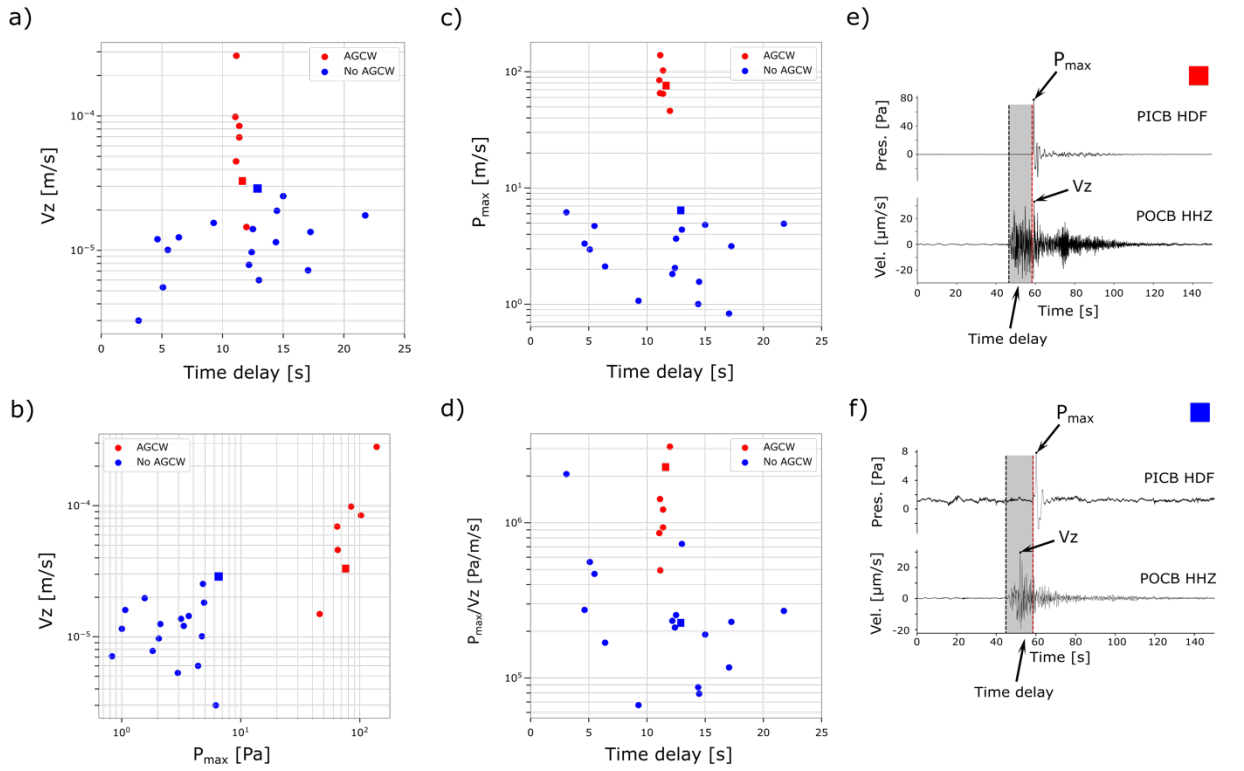

Figure 10. Comparison between a) Peak vertical velocity amplitude Vz vs. time delay, b) peak pressure amplitude P_{max} vs. time delay, c) Vz vs. P_{max}, and d) the ratio between P_{max} and Vz. The time delay is the absolute value of the difference between the seismic phase arrival time and the infrasound phase arrival time. The red dots correspond to the events whose seismic phase has air-to-ground coupled waves (AGCW), and the blue dots correspond to seismic events without AGCW. An example of unfiltered infrasound and vertical seismic signals recorded in Cruz Blanca site associated with explosions occurred in September 2021 with e) an ACGW and f) no AGCW are shown in the right column. The values of e) and

572 f) events in plots a) - d) are pointed as red and blue squares respectively. The black line shows the onset
573 of the seismic signal, the red line shows the onset of the infrasound signal, and the gray area shows the
574 time delay between the seismic signal and the infrasound signal. The black arrows point to the maximum
575 values of pressure P_{max} and vertical velocity V_z used to create the scatter plots.
576
577 Figure 10 summarizes these automated detections along with the associated infrasound
578 signals by showing the comparison between events using the peak vertical velocity value,
579 the peak pressure value, the time delay between seismic and infrasound signal arrival
580 times (Ishii et al., 2019; Matoza et al., 2022; Ripepe et al., 2001, 2005), and the peak
581 infrasonic pressure to peak seismic velocity amplitude ratio P/Vz (Matoza et al., 2005;
582 Matoza et al., 2022). In all T1-similar detections, we observe a clear AGCW, the peak
583 pressures lie between 40 – 110 Pa, and the arrival time is around 12 s. In contrast, the
584 T2-similar peak pressures do not surpass 10 Pa, and the time delays are less clear due
585 to uncertainties in the infrasound wave identification (Figure 10b). Nevertheless, it is clear
586 that the AGCW phase is heavily dependent on the size of the eruption, and smaller
587 explosions do not present seismo-acoustic coupling even in the closest stations to the
588 volcano.
589
590 **Conclusions**
591
592 In this work, we presented an overview of the deployment and the observations of the
593 temporal seismo-acoustic network PoPiNet from August 2021 through May 2022. This
594 network is the first ever high-quality high-broadband (0.01 – 200 Hz; 400 Hz sampling
595 rate) seismic-acoustic network deployed around Popocatépetl volcano. PoPiNet

consisted of five sites installed around Popocatépetl within a source-receiver distance of 4 – 25 km from the crater. Analyzing the performance of all stations through the operation time, we observed in most of the stations that the traces present anthropogenic and wind noise. Infrasound signatures show spectral peaks within the 0.2 – 5.0 Hz range associated to the explosions in all stations. The frequency contents of the traces extended up to the sub-bass (20 - 60 Hz) and bass (60 – 250 Hz) ranges. However, infrasonic tremor, observed at the closest stations to the volcano, is difficult to identify, pointing out the need to evaluate the effects of the wind's direction and velocity. In all stations, we observed explosions related to seismo-acoustic signals. The AGCW is present in those events associated with moderate and larger explosions. The coherence estimation revealed that the coupling is present at frequencies up to 25 Hz at the closest stations to the volcano. The coupling is limited to lower frequencies (up to 5 Hz) when increasing the source-receiver distance. Previous studies have reported similarity in seismic signal characteristics, including LP and VLP waveforms (Arciniega–Ceballos et al., 1999, 2003, 2008, 2012; Chouet et al., 2005; Matoza et al., 2019; Mendo–Pérez et al., 2021). Future work aims to characterize and locate seismo-acoustic sources and tremor signals related to the eruptive activity of Popocatépetl volcano, from degassing to Vulcanian explosions.

Data and Resources

Infrasound data is converted to mseed format using the cube_conversion Python program from uafgeotools package (https://github.com/uafgeotools/cube_conversion) and modified using the infrasound and dataloggers acquisition parameters. We use

Nanometrics Apollo Project software to download and convert seismic data into SAC and mseed formats. Data processing was done using Numpy (Harris et al., 2020), Scipy (Virtanen et al., 2020), and Obspy (Beyreuther et al., 2010; Megies, 2011; Krischer, 2015) libraries. Popocatépetl volcano maps were done using PyGMT (Tian et al., 2024), and we plot the data using Matplotlib (Hunter et al., 2007). Multitaper estimation was performed using the Prieto (2022) Python code (https://github.com/gaprieto/multitaper). The wind speed and direction data recorded by the meteorological station Altzomoni was obtained from the Red Universitaria de Observatorios Atmosfericos (RUOA by its acronym in Spanish) webpage (https://www.ruoa.unam.mx/index.php?page=estaciones&id=2) from the Institute of Atmospheric Sciences and Climate Change, UNAM. Population data was obtained from Secretaría de Desarrollo Agrario, Territorial e Urbano (https://www.gob.mx/sedatu), and the Instituto Nacional de Estadistica, Geografia e Informatica (https://en.www.inegi.org.mx/). The Supplemental Material of this paper includes more examples of the calculations obtained from the rest of the stations of PoPiNet network, and tables related to the equipment characteristics and the detections from template matching algorithm.

Declaration of Competing Interests

The authors acknowledge there are no conflicts of interest recorded.

642 **Acknowledgments**

643

644 This work was possible thanks to the funding provided by the UNAM DGAPA-PAPIIT
645 projects IN108219, IN105216, and IN104823, and the UC-MEXUS project “Seismic and
646 infrasound signature of explosive eruptions at Popocatépetl volcano” with identification
647 number CN-18-51. This work was also partially supported by NSF grants EAR-1847736
648 and EAR-1620576 to RSM. The authors also want to express their gratitude to the
649 academics of the Institute of Geophysics, UNAM: M Calò from and his research team,
650 who provided the seismic data from POBV station and gave us access to their station, to
651 L Salazar Tlazcani and M Diaz, who support us with the installation and maintenance of
652 the stations. We are grateful to the administrative personnel and wardens of Izta-Popo
653 National Park, to the police from Estado de México, to Efrain and Liduvina Posadas and
654 all the personnel from Buenavista Touristic Village, to Edgardo and his personnel from
655 San Pedro Nexapa Touristic Village, to the late Leticia Vazquez who kindly opened us
656 her home to install Tochimilco site, and W Junghanns and all his personnel who kindly
657 opened us the doors of his hotel “Hotel Esmeralda” in Atlixco, Puebla. We thank Leighton
658 Watson and Jake Anderson for their comments that helped improve this paper.

659

660

661

662

663

664

References

Alatorre-Ibargüengoitia, M. A., and Delgado-Granados, H. (2006). Experimental determination of drag coefficient for volcanic materials: Calibration and application of a model to Popocatépetl volcano (Mexico) ballistic projectiles. Geophys. Res. Lett., 33, no. 8. https://doi.org/10.1029/2006GL026195

Alatorre-Ibargüengoitia, M. A., Delgado-Granados, H., and Dingwell, D. B. (2012). Hazard map for volcanic ballistic impacts at Popocatépetl volcano (Mexico). Bull. Volcanol., 74, 2155 - 2169. https://doi.org/10.1007/s00445-012-0657-2

Alatorre-Ibargüengoitia, M. A., Arciniega-Ceballos, A., Linares López, C., Dingwell, D. B., and Delgado-Granados, H. (2019). Fragmentation behavior of eruptive products of Popocatépetl volcano: an experimental contribution. Geofísica Internacional, 58, no. 1, 49 - 72. https://www.scielo.org.mx/scielo.php?pid=S0016-71692019000100049&script=sci_arttext&tlng=en

Arámbula – Mendoza, R., Valdes-Gonzalez, C., Varley, N., Reyes-Pimentel, T. A., and Juarez – Garcia, B. (2016). Tremor and its duration-amplitude distribution at Popocatépetl volcano, Mexico. Geophys. Res. Lett., 43, no. 17, 8994 – 9001. https://doi.org/10.1002/2016GL070227

Arciniega-Ceballos, A., Chouet, B. A., and Dawson, P. (1999). Very long-period signals associated with Vulcanian Explosions at Popocatepetl Volcano, Mexico. Geophys. Res. Lett., 26, no. 19, 3013-3016. https://doi.org/10.1029/1999GL005390

Arciniega-Ceballos, A., Chouet, B., and Dawson, P. (2003). Long-period events and tremor at Popocatepetl volcano (1994–2000) and their broadband characteristics. Bull. Volcanol., 65, 124 - 135. https://doi.org/10.1007/s00445-002-0248-8

692 Arciniega-Ceballos, A., Chouet, B., Dawson, P., and Asch, G. (2008). Broadband seismic measurements
693 of degassing activity associated with lava effusion at Popocatépetl Volcano, Mexico. J. Volcanol. Geoth.
694 Res., 170, no. 1 - 2, 12 - 23. https://doi.org/10.1016/j.jvolgeores.2007.09.007
695
696 Arciniega-Ceballos, A., Dawson, P., and Chouet, B. A. (2012). Long period seismic source characterization
697 at Popocatépetl volcano, Mexico. Geophys. Res. Lett., 39, no. 20. https://doi.org/10.1029/2012GL053494
698
699 Arciniega-Ceballos, A., Valdes-Gonzalez, C., and Dawson, P. (2000). Temporal and spectral
700 characteristics of seismicity observed at Popocatepetl volcano, central Mexico. J. Volcanol. Geoth.
701 Res., 102, no. 3-4, 207-216. https://doi.org/10.1016/S0377-0273(00)00188-8
702
703 Beyreuther, M., Barsch, R., Krischer, L., Megies, T., Behr, Y., and Wassermann, J. (2010). ObsPy: A Python
704 toolbox for seismology. Seismol. Res. Let., 81, no. 3, 530-533. https://doi.org/10.1785/gssrl.81.3.530
705
706 Bishop, J. W., Haney, M. M., Fee, D., Matoza, R. S., McKee, K. F., and Lyons, J. J. (2023). Back-azimuth
707 Estimation of the Air-to-Ground Coupled Infrasound from Transverse Coherence Minimization. The Seismic
708 Record, 3, no. 4, 249 – 258. https://doi.org/10.1785/0320230023
709
710 Bowman, J. R., Baker, G. E., and Bahavar, M. (2005). Ambient infrasound noise. Geophys. Res. Lett., 32,
711 no. 9. https://doi.org/10.1029/2005GL022486
712
713 Caplan-Auerbach, J., Bellesiles, A., and Fernandes, J. K. (2010). Estimates of eruption velocity and plume
714 height from infrasonic recordings of the 2006 eruption of Augustine Volcano, Alaska. J. Volcanol. Geoth.
715 Res., 189, no. 1 - 2, 12 – 18. https://doi.org/10.1016/j.jvolgeores.2009.10.002
716
717 Chouet, B. (2003). Volcano Seismology. Pure Appl. Geophys., 160, 739 – 788.
718 https://doi.org/10.1007/PL00012556

Chouet, B., Dawson, P., and Arciniega-Ceballos, A. (2005). Source mechanism of Vulcanian degassing at Popocatépetl Volcano, Mexico, determined from waveform inversions of very long period signals. J. Geophys. Res. B. Solid Earth Planets, 110, no. B7. https://doi.org/10.1029/2004JB003524

Chouet, B. A., and Matoza, R. S. (2013). A multi-decadal view of seismic methods for detecting precursors of magma movement and eruption. J. Volcanol. Geoth. Res., 252, 108 – 175. https://doi.org/10.1016/j.jvolgeores.2012.11.013

Cruz-Atienza, V. M., Pacheco, J. F., Singh, S. K., Shapiro, N. M., Valdés, C., and Iglesias, A. (2001). Size of Popocatepetl Volcano explosions (1997-2001) from waveform inversion. Geophys. Res. Lett., 28, no. 21, 4027 – 4030. https://doi.org/10.1029/2001GL013207

De Angelis, S., Fee, D., Haney, M., and Schnider, D. (2012). Detecting hidden volcanic explosions from Mt. Cleveland Volcano, Alaska, with infrasound and ground-coupled airwaves. Geophys. Res. Lett., 39, no. 21. https://doi.org/10.1029/2012GL053635

De la Cruz-Reyna, S., and Siebe, C. (1997). The giant Popocatépetl stirs. Nature, 388, no. 277. https://doi.org/10.1038/40749

Dybing, S. N., Ringler, A. T., Wilson, D. C., and Anthony, R. E. (2019). Characteristics and Spatial Variability of Wind Noise on Near-Surface Broadband Seismometers. Bull. Seismol. Soc. Am., 109, no. 3, 1082 – 1098. https://doi.org/10.1785/0120180227

Fee, D., & Matoza, R. S. (2013). An overview of volcano infrasound: from Hawaiian to Plinian, local to global. J. Volcanol. Geoth. Res., 249, 123 – 139. https://doi.org/10.1016/j.jvolgeores.2012.09.002

746 Fee, D., Garces, M., Patrick, M., Chouet, B., Dawson, P., and Swanson, D. (2010). Infrasonic harmonic
747 tremor and degassing bursts from Halema'uma'u Crater, Kilauea Volcano, Hawaii. J. Geophys. Res. B
748 Solid Earth Planets, 115, no. B11. https://doi.org/10.1029/2010JB007642
749
750 Fee, D., Garces, M., and Steffke, A. (2010). Infrasound from Tungurahua Volcano 2006 – 2008:
751 Strombolian to Plinian eruptive activity. J. Volcanol. Geoth. Res., 193, no. 1 - 2, 67 – 81.
752 https://doi.org/10.1016/j.jvolgeores.2010.03.006
753
754 Fee, D., Yokoo, A., and Johnson, J. B. (2014). Introduction to an Open Community Infrasound Dataset from
755 the Actively Erupting Sakurajima Volcano, Japan. Seismol. Res. Lett., 85, no. 6, 1151 – 1162.
756 https://doi.org/10.1785/0220140051
757
758 Ferrari, L., Orozco-Esquivel, T., Manea, V., and Manea, M. (2012). The dynamic history of the Trans-
759 Mexican Volcanic Belt and the Mexico subduction zone. Tectonophysics, 522-523, 122 – 149.
760 https://doi.org/10.1016/j.tecto.2011.09.018
761
762 Garcés, M., Iguchi, M., Ishihara, K., Morrissey, M., Sudo, Y. and Tsutsui, T. (1999). Infrasonic precursors
763 to a Vulcanian Eruption at Sakurajima Volcano, Japan. Geophys. Res. Lett., 26, no. 16, 2537 – 2540.
764 https://doi.org/10.1029/1998GL005327
765
766 Gibbons, S. J., and Ringdal, F. (2006). The detection of low-magnitude seismic events using array-based
767 waveform correlation. Geophys. J. Int., 165, no. 1, 149 – 166. https://doi.org/10.1111/j.1365-
768 246X.2006.02865.x
769
770 Gómez-Vazquez, A., De la Cruz-Reyna, S., and Mendoza-Rosas, A. T. (2016). The ongoing dome
771 emplacement and destruction cyclic process at Popocatépetl volcano, Central Mexico. Bull. Volcanol., 78,
772 no. 58. https://doi.org/10.1007/s00445-016-1054-z
773

774 Harris, C. R., Millman, K. J., van der Walt, S. J., Gommers, R., Virtanen, P., Cournapeau, D., Wieser, E.,
775 Taylor, J., Berg, S., Smith, N. J., Kern, R., Picus, M., Hoyer, S., van Kerkwijkm M. H., Brett, M., Haldane,
776 A., Fernandez del Rio, J., Wiebe, M., Peterson, P., Gerard-Marchant, P., Sheppard, K., Reddy, T.,
777 Weckesser, W., Abbasi, H., Gohlkem C., and Oliphant, T. E. (2020). Array programming with NumPy.
778 Nature, 585, 357 – 362. https://doi.org/10.1038/s41586-020-2649-2
779
780 Hunter, J. D. (2007). Matplotlib: A 2D Graphics Environment. Computing in Science and Engineering, 9, no.
781 3, 90 – 95. https://doi.org/10.1109/MCSE.2007.55
782
783 Ichihara, M., Takeo, M., Yokoo, A., Oikawa, J., and Ohminato, T. (2012). Monitoring volcanic activity using
784 correlation patterns between infrasound and ground motion. Geophys. Res. Lett., 39, no. 4.
785 https://doi.org/10.1029/2011GL050542
786
787 Ichihara, M., Yamakawa, K., and Muramatsu, D. (2021). A simple method to evaluate the air-to-ground
788 coupling efficiency: a tool helping the assessment of seismic/infrasonic energy partitioning during an
789 eruption. Earth Planets Space, 73, no. 180. https://doi.org/10.1186/s40623-021-01510-4
790
791 Iezzi, A. M., Matoza, R. S., Bishop, J. W., Bhetanabhotla, S., and Fee, D. (2022). Narrow-Band Least-
792 Squares Infrasound Array Processing. Seismol. Res. Lett., 95, no. 5, 2818 – 2833.
793 https://doi.org/10.1785/0220220042
794
795 Johnson, J. B., and Ripepe, M. (2011). Volcano Infrasound: A review. J. Volcanol. Geoth. Res., 206, no. 3
796 - 4, 61 – 69. https://doi.org/10.1016/j.jvolgeores.2011.06.006
797
798 Krischer, L., Megies, T., Barsch, R., Beyreuther, M., Lecocq, T., Caudron, C., and Wassermann, J. (2015).
799 ObsPy: a bridge for seismology into the scientific Python ecosystem. Comput. Sci. Discov., 8, no. 1.
800 https://iopscience.iop.org/article/10.1088/1749-4699/8/1/014003/meta
801

802 Macias, J. L., Arce, J. L., García – Tenorio, F., Sosa-Ceballos, G., and Gardner, J. E. (2020). Source and
803 behavior of pyroclastic density currents generated by the Vulcanian-style explosions of Popocatépetl
804 volcano (Mexico) on 22 January 2001. J. Volcanol. Geoth. Res., 406, no. 107071.
805 https://doi.org/10.1016/j.jvolgeores.2020.107071
806
807 Maher, S. P., Matoza, R. S., Jolly, A., de Groot-Hedlin, C., Gee, K. L., Fee, D., and Iezzi, A. M. (2022).
808 Evidence for near-source nonlinear propagation of volcano infrasound from Strombolian explosions at
809 Yasur volcano, Vanuatu. Bull. Volcanol., 84, 41. https://doi.org/10.1007/s00445-022-01552-w
810
811 Martin-Del Pozzo, A. L., Rodriguez, A., and Portocarrero, J. (2016). Reconstructing 800 years of historical
812 eruptive activity at Popocatépetl Volcano, Mexico. Bull. Volcanol., 78, no. 18.
813 https://doi.org/10.1007/s00445-016-1010-y
814
815 Matoza, R. S., Arciniega-Ceballos, A., Sanderson, R. W., Mendo-Pérez, G., Rosado-Fuentes, A., and
816 Chouet, B. A. (2019). High-broadband Seismoacoustic signature of Vulcanian explosions at Popocatépetl
817 volcano, Mexico. Geophys. Res. Lett., 46, no. 1, 148-157. https://doi.org/10.1029/2018GL080802
818
819 Matoza, R.S., Chouet, B. A., Dawson, P. B., Shearer, P. M., Haney, M. M., Waite, G. P., Moran, S. C.,
820 and Mikesell, T. D. (2015). Source mechanism of small long-period events at Mount St. Helens in July
821 2005 using template matching, phase-weighted stacking, and full-waveform inversion, J. Geophys. Res.
822 B Solid Earth Planets, 120, 6351–6364. https://doi.org/10.1002/2015JB012279
823
824 Matoza, R. S., Chouet, B. A., Jolly, A. D., Dawson, P. B., Fitzgerald, R. H., Kennedy, B. M., ... and Cevuard,
825 S. (2022). High-rate very-long-period seismicity at Yasur volcano, Vanuatu: source mechanism and
826 decoupling from surficial explosions and infrasound. Geophys. J. Int., 230, no. 1, 392-426.
827 https://doi.org/10.1093/gji/ggab533
828

Matoza, R. S., and Fee, D. (2014). Infrasonic component of volcano-seismic eruption tremor. Geophys. Res. Lett., 41, no. 6, 1964 – 1970. https://doi.org/10.1002/2014GL059301

Matoza, R. S., and Fee, D. (2018). The inaudible rumble of volcanic eruptions. Acoust. Today, 14, no. 1. https://escholarship.org/content/qt4vn1j277/qt4vn1j277.pdf

Matoza, R. S., Fee, D., Garcés, M. A., Seiner, J. M., Ramón, P. A., and Hedlin, M. A. H. (2009a). Infrasonic jet noise from volcanic eruptions. Geophys. Res. Lett., 36, no. 8. https://doi.org/10.1029/2008GL036486

Matoza, R. S., Fee, D., Neilsen, T. B., Gee, K. L., and Ogden, D. E. (2013). Aeroacoustics of volcanic jets: Acoustic power estimation and jet velocity dependence. J. Geophys. Res. B. Solid Earth Planets, 118, no. 12, 6269 – 6284. https://doi.org/10.1002/2013JB010303

Matoza, R. S., Garcés, M. A., Chouet, B. A., D'Auria, L., Hedlin, M. A. H., De Groot-Hedlin, C., and Waite, G. P. (2009). The source of infrasound associated with long-period events at Mount St. Helens, J. Geophys. Res. B. Solid Earth Planets, 114, no. B4. https://doi.org/10.1029/2008JB006128

Matoza, R. S., Hedlin, M. A. H., and Garcés, M. A. (2007). An infrasound array study of Mount St. Helens. J. Volcanol. Geoth. Res., 160, no. 3 - 4, 249 – 262. https://doi.org/10.1016/j.jvolgeores.2006.10.006

Matoza, R. S., and Roman, D. (2022). One hundred years of advances in volcano seismology and acoustics. Bull. Volcanol., 84, no. 86. https://doi.org/10.1007/s00445-022-01586-0

McNamara, D. E., and Buland, R. P. (2004). Ambient Noise Levels in the Continental United States. Bull. Seismol. Soc. Am., 94, no. 4, 1517-1527. https://doi.org/10.1785/012003001

McNutt, S. R. (2005). Volcanic seismology. Annual Review of the Earth and Planetary Sciences, 33, 461 - 491. https://doi.org/10.1146/annurev.earth.33.092203.122459

857

858 Megies, T., Beyreuther, M., Barsch, R., Krischer, L., and Wassermann, J. (2011). ObsPy – What can it do
859 for data centers and observatories?. Annals of Geophysics, 54, no. 1, 47 – 58. https://doi.org/10.3929/ethz-
860 b-000130217

861

862 Mendo-Pérez, G., Arciniega-Ceballos, A., Matoza, R. S., Rosado-Fuentes, A., Sanderson, R. W., and
863 Chouet, B. A. (2021). Ground-coupled airwaves template match detection using broadband seismic records
864 of explosive eruptions at Popocatépetl volcano, Mexico. J. Volcanol. Geoth. Res., 419, no. 107378.
865 https://doi.org/10.1016/j.jvolgeores.2021.107378

866

867 Morrissey, M. M., and Chouet, B. A. (1997). A numerical investigation of choked flow dynamics and its
868 application to the triggering mechanism of long-period events at Redoubt Volcano, Alaska. J. Geophys.
869 Res. B. Solid Earth Planets, 102, no. B4, 7965 – 7983. https://doi.org/10.1029/97JB00023

870

871 Prieto, G. (2022). The Multitaper Spectrum Analysis Package in Python. Seismol. Res. Lett., 93, no. 3,
872 1922 – 1929. https://doi.org/10.1785/0220210332

873

874 Petersen, T., and McNutt, S. R. (2007). Seismo-acoustic signals associated with degassing explosions
875 recorded at Shishaldin Volcano, Alaska, 2003 – 2004. Bull. Volcanol., 69, 527 – 536.
876 https://doi.org/10.1007/s00445-006-0088-z

877

878 Prieto, G., Parker, R., and Vernon III, F. (2009). A Fortran 90 library for multitaper spectrum analysis.
879 Comput. Geosci., 35, no. 8, 1701 – 1710. https://doi.org/10.1016/j.cageo.2008.06.007

880

881 Ramirez-Uribe, I., Siebe, C., Chevrel, M. O., Ferres, D., and Salinas, S. (2022). The late Holocene Nealtican
882 lava-flow field, Popocatépetl volcano, central Mexico: Emplacement dynamics and future hazards. Geol.
883 Soc. Am. Bull., 134, no. 11 - 12, 2745 – 2766. https://doi.org/10.1130/B36173.1

884

885 Ripepe, M., Poggi, P., Braun, T., and Gordeev, E. (1996). Infrasonic waves and volcanic tremor at Stromboli.
886 Geophys. Res. Lett., 23, no. 2, 181 – 184. https://doi.org/10.1029/95GL03662
887
888 Roman, D. C. (2017). Automated detection and characterization of harmonic tremor in continuous seismic
889 data. Geophys. Res. Lett., 44, no. 12, 6065 – 6073. https://doi.org/10.1002/2017GL073715
890
891 Sanderson, R. W., Matoza, R. S., Haymon, R. M., and Steidl, J. H. (2021). A Pilot Experiment on Infrasonic
892 Lahar Detection at Mount Adams, Cascades: Ambient Infrasound and Wind-Noise Characterization at a
893 Quiescent Stratovolcano. Seismol. Res. Lett., 92, no. 5, 3065 – 3086. https://doi.org/10.1785/0220200361
894
895 Virtanen, P., Gommers, R., Oliphant, T. E., Haberland, M., Reddy, T., Cournapeau, D., ... and Van Mulbregt,
896 P. (2020). SciPy 1.0: fundamental algorithms for scientific computing in Python. Nature methods, 17, no. 3,
897 261-272.
898
899 Woulff, G., and McGetchin, T. R. (1976). Acoustic Noise from Volcanoes: Theory and Experiment. Geophys.
900 J. Int., 45, no. 3, 601 – 616. https://doi.org/10.1111/j.1365-246X.1976.tb06913.x
901
902 Wright, R., De La Cruz-Reyna, S., Harris, A., Flynn, L., and Gomez-Palacios, J. J. (2002). Infrarred satellite
903 monitoring at Popocatépetl: Explosions, exhalations, and cycles of dome growth. J. Geophys. Res. B. Solid
904 Earth Planets, 107, no. B8, 2-1 – 2-16. https://doi.org/10.1029/2000JB000125
905
906 Yamada, T., Aoyama, H., Nishimura, T., Iguchi, M., and Hendrasto, M., (2016). Volcanic eruption volume
907 flux estimations from very long period infrasound signals. Geophys. Res. Lett., 44, no. 1, 143 – 151.
908 https://doi.org/10.1002/2016GL071047
909
910 Yokoo, A., Tameguri, T., and Iguchi, M. (2009). Swelling of a lava plug associated with a Vulcanian eruption
911 at Sakurajima Volcano, Japan, as revealed by infrasound record: case study of the eruption on January 2,
912 2007. Bull. Volcanol., 71, 619 – 630. https://doi.org/10.1007/s00445-008-0247-5

Authors' mailing address list

Gerardo Mendo-Perez: 1-1-1 Yayoi, Bunkyo city, Tokyo, Japan 113-0032

Alejandra Arciniega-Ceballos: Circuito de la Investigación Científica s/n, Ciudad Universitaria, Alcaldía Coyoacán, Ciudad de México 04510.

Robin S. Matoza: Department of Earth Science, Webb Hall MC 9630, UC Santa Barbara, Santa Barbara, CA 93106.

Alejandro Rosado-Fuentes: Circuito de la Investigación Científica s/n, Ciudad Universitaria, Alcaldía Coyoacán, Ciudad de México 04510.

Richard W. Sanderson: Bústaðavegur 9, 105 Reykjavík, Iceland

Miranda R. Claypool: Department of Earth Science, Webb Hall MC 9630, UC Santa Barbara, Santa Barbara, CA 93106.